ROYAL SOCIETY
OF CHEMISTRY

PAPER

Check for updates

The effect of lithium on structural and luminescence performance of tunable light-emitting nanophosphors for white LEDs

Sanjeeb Limbu, [a] Laishram Robindro Singh [*a] and Gunadhor Singh Okram [b]

Li^+ incorporated tunable Y_2O_3:Eu^{3+} red-emitting nanophosphors were synthesized using a wet chemical method. The effect of Li^+ on structural and luminescence properties of the nanophosphors were studied in detail. The structural results exhibited that nanophosphors have a body-centered cubic (I) phase with point group symmetry $m\bar{3}$. No additional impurity peaks were observed within the range of the XRD pattern due to the Li^+ ion. FTIR spectra reveal the formation of the pure and crystalline structure of the nanophosphors. TEM results show the prepared nanophosphors were highly crystalline and polycrystalline in nature. PL studies show the highly enhanced emission band due to the flux effect, greatly improved crystallinity caused by the Li^+ ion, and the different excitation wavelengths. The most intense luminescence band was observed at 612 nm for red emission ascribed to the $^5D_0 \rightarrow {}^7F_2$ transition of Eu^{3+} ion upon 254, 393, and 465 nm excitations in the C_{3i} and C_2 symmetry site of Y_2O_3 respectively. The highly enhanced emission band was observed under excitation at 254 nm and is 6.9 and 3.67 times higher than the emission band excited at 393 and 466 nm, respectively. The average lifetime also varies with different concentrations of Li^+ ions. The chromaticity color coordinates, CCT values, were tuned in the red region of the color space. Hence, the results indicate that the prepared nanophosphor can be used as a red component to construct the white light for light-emitting diode applications.

1. Introduction

Over the last several decades, rare earth (RE) doped luminescence materials have attracted broad research interest, because of their potential application in various fields. Eu^{3+} activated Y_2O_3 materials have been widely used as a red-emitting nanophosphor in the white-light-emitting diodes, plasma display panels (PDPs), field emission displays (FEDs), and cathode ray tube (CRTs).[1–3] They have high luminous efficiency, excellent luminescence properties, high quantum efficiency, color purity, high brightness, and good atmospheric stability.[4] This nanophosphor based LED can be used to replace incandescent and fluorescent lamps due to their longer lifetime, lower energy consumption and eco-friendly behavior. They don't use toxic elements such as mercury as an excitation light source. The Eu^{3+} ion can reveal both the divalent and trivalent valence state among the various RE elements. Therefore, Eu^{3+} doped phosphors are used to produce blue, green, and red luminescence efficiently based on various host materials.[5] The Eu^{3+} ion exhibits a prominent red emission band due to the $^5D_0 \rightarrow {}^7F_2$ transition at about 612 nm and is used as a red component for

white LED fabrication.[6] Because of the special character, Eu^{3+} ion has been widely used as an activator in different nanophosphors.

It is well known that Li^+ ion as a codopant is widely used to improve luminescence efficiency and enhanced the emission band intensity. The important role of the Li^+ ion is to serve as flux materials, resulting in the higher crystallinity and growth of the crystallite size.[7,8] Wang *et al.* reported that photoluminescence intensity of Y_2O_3:Eu^{3+} thin-films phosphors were greatly improved by the addition of Li^+ ion.[9] The phosphor emission band intensity was enhanced by around 3.5 times with Li^+ ions. The reason for highly enhancement photoluminescence intensity was improved crystallinity, increase optical volume, and changes the concentration of oxygen vacancies caused by the flux effect of Li^+ ion. Li Yongquiang *et al.* found that the enhancement of photoluminescence intensity of Y_2O_3:5% Eu^{3+}, x% Li^+ phosphor thin film, from 0–15% with increasing Li^+ doping concentration and then declines with Li^+ doping further due to the creation of oxygen vacancies in the phosphors.[10] Very recently, Ashim *et al.* developed the Froster resonance energy transfer (FRET) based on rare earth material free white light-emitting colloidal luminescent due (LD) namely DCM@N-GQDs$_{0.7}$ with an energy efficiency ~30%. The F-LED exhibits an emission overlapping (56%) with the solar spectrum (AM 1.5) in the visible region

aDepartment of Nanotechnology, North-Eastern Hill University, Shillong-793022, India. E-mail: lrsingh@nehu.ac.in; Tel: +91-364-2723903

bUGC-DAE Consortium for Scientific Research (CSR), Indore-452017, India

which is two times higher than the commercial LED. They also tuned the PL emission in the blue and red regions by changing the D-A ratio.[11] Quan *et al.* has fabricated a white light-emitting diode by mixing S, N-codoped oil-soluble carbon dots with epoxy and drop-casting the mixture on the gallium nitride (GaN) surface-based blue chips. This shows the excellent color property to fabricate WLED. The CCT, CIE and CRI values were found to be 5389 K, (0.33, 0.30) and 88.38, respectively.[12] The quantum yield optimized of white-emitting CdSe QDs up to 22% by controlling the synthesis parameters of reaction time and temperature. Where the broad emission band was observed in the visible region and the color rendering index, luminous efficiency showed up to 89 and 11.7 lm W^{-1}, respectively.[13]

In this work, we have analyzed the enhancement of emission intensity for Y$_2$O$_3$:4 at% Eu^{3+} nanophosphors, prepared by a wet chemical method with xLi$^+$ (x = 0.5, 1, 3, 5, 7, 9 at%) co-doping from a new angle. This is well known that the variation of luminescence intensity depends on the doping concentration. With the increase of the doping concentration, the luminescent intensity enhances at first then drops down quickly. This is due to the concentration quenching effect, and the inflection point is known as the concentration quenching threshold. The concentration quenching phenomenon results from the energy transfer within neighboring ions. Here we have only investigated the effect of the codoped Li$^+$ ion for the structural study and compare the enhances the luminescent intensity of Y$_2$O$_3$:Eu^{3+} nanophosphor under various excitation wavelengths. In the case of our study, PL emission intensity greatly increased from 0.5 to 7 at% codoping of Li$^+$ concentration after that it decreased. Thus the 7 at% codoping concentration possessed the strongest luminescence emission intensity as a concentration quenching threshold. The structural study shows that no additional impurity peaks were exhibited within the whole range of the XRD pattern due to the Li$^+$ codopant. Besides, the effect of Li$^+$ on the crystal structure, internal morphology, and colorimetric performance are studied in detail.

2. Experimental section

2.1. Materials and methods

A series of xLi$^+$ (x = 0.5, 1, 3, 5, 7, 9 at%) co-activated Y$_2$O$_3$:4 at% Eu^{3+} nanophosphors were prepared by wet chemical methods.[14] For the preparation of the nanophosphor, yttrium(III) acetate hydrate (CH$_3$·CO$_2$)$_3$Y·xH$_2$O (Alfa Aesar 99.99%), europium(III) oxide (Eu$_2$O$_3$) (Sigma Aldrich 99.99%), and lithium acetate (C$_2$H$_3$LiO$_2$) (Sigma-Aldrich, 99.95%, purity) were used as starting materials. Initially, 0.5 g yttrium(III) acetate hydrate (CH$_3$·CO$_2$)$_3$Y·xH$_2$O (Alfa Aesar 99.99%) and the calculated amount of (4 at%) Eu$_2$O$_3$ (Sigma Aldrich 99.99%) was mixed with 10 ml of dilute hydrochloric acid. The mixtures were stirred vigorously to get a clear solution. The solution was evaporated many times in double distilled water to remove excess acids from the solution. The solution was poured into a 250 ml round bottom flask having a condenser. Polyethylene glycol of 25 ml was added and warms the solution until it got clear. Then, 1 M strength sodium hydroxide (AR) was added into the observed clear solution and heated continuously the mixture up to 140 °C. The solution was

observed as foggy white precipitate and continued the reaction for three hours. To remove the additional ligands, the forming white precipitate was washed several times using double distilled water and methanol under the centrifugation process. Finally, the residue was collected and considered as Y$_2$O$_3$:4 at% Eu^{3+} nanoparticles. To incorporate xLi$^+$ ions in Y$_2$O$_3$:4 at% Eu^{3+}, lithium acetate (C$_2$H$_3$LiO$_2$) (Sigma-Aldrich, 99.95%, purity) was initially dissolved in double distilled water to get Li$^+$ ions and is simply added into the mixture of Y^{3+} and Eu^{3+} and follows the same procedure were followed as to prepare Y$_2$O$_3$:4 at% Eu^{3+} nanoparticles. The prepared sample was annealed at 900 °C for 3 h. These synthesized nanomaterials were kept continuously in the furnace for cool down to room temperature and ground for further characterization to observe the structural and luminescence properties.

2.2. Materials characterization

X-ray diffraction (XRD) data were obtained by Explorer, GNR Instrument and Analysis, Italy using Cu Kα radiation source and a monochromatic wavelength (λ = 1.5406 Å) operating at 40 kV tube voltage and 35 mA tube current with 2θ angle ranging from 10 to 80°. The Rietveld refinement,[15] quantitative structural analysis was conducted using FullProf Suite,[16] software package. The crystal structure and the profile matching parameters data of cubic Y$_2$O$_3$ were taken from Crystallographic Open Database (COD). The internal morphology and particle size micrographs were taken by a high-resolution transmission electron microscopy (HRTEM) which was performed with (JEOL, JEM-2100) electron microscope with a tungsten filament gun operating at an accelerating voltage 200 kV. The samples for TEM were prepared by drying a drop of methanol ultrasonically dispersion of 5 mg sample for 1 h on a carbon-coated Cu-grid. The selected area electron diffraction (SAED) patterns were also obtained. The Fourier transform infrared (FTIR) spectra of the nanophosphor were monitored within the mid-IR region using KBr pellet techniques by Bruker (Model: Alpha) spectrometer. All photoluminescence (PL) measurements were
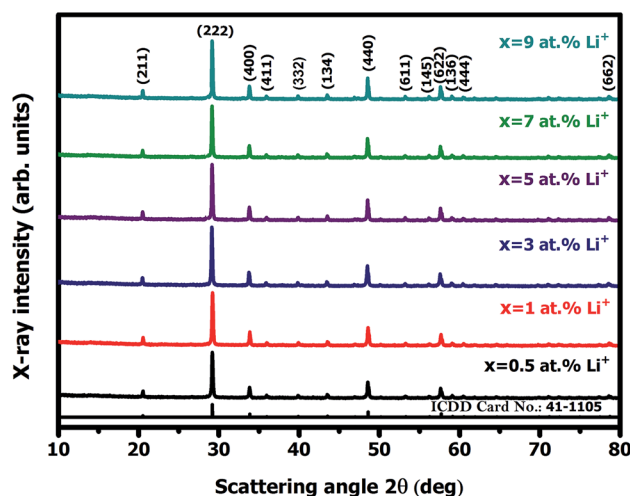

Fig. 1 X-ray diffraction (XRD) pattern of Y$_2$O$_3$:4 at% Eu^{3+}, xLi$^+$ (x = 0.5, 1, 3, 5, 7, 9 at%) nanophosphors.

observed on a Hitachi F-7000 Fluorescence Spectrophotometer at room temperature with slit width kept open for 3 nm, having a 150 W Xe arc lamp as an excitation light source. The Commission Internationale de l'Éclairage (CIE) 1931 color calculator was used to evaluating the chromaticity color coordinates (x, y) from the PL emission spectra.

3. Results and discussion

3.1. Structural characterization

3.1.1. Qualitative X-ray diffraction analysis. Fig. 1 represents the X-ray diffraction (XRD) patterns of Y_2O_3:4 at% Eu^{3+},

xLi^+ ($x = 0.5, 1, 3, 5, 7, 9$ at%) nanophosphors. All the diffraction peaks are in good agreement with the standard International Centre for Diffraction Data (ICDD) Card No. 41-1105 corresponding to the cubic structure of Y_2O_3 with $Ia\bar{3}$ (Number 206, $Z = 16$) space group. No additional peaks of other phases were observed in the XRD diffraction pattern. It indicates Li^+ ion was incorporated into the host lattice, there is no effect observed on the XRD pattern. The average crystallite size (D) of the prepared sample was estimated from the prominent diffraction peak of (222) plane using Debye–Scherrer equation:[17]

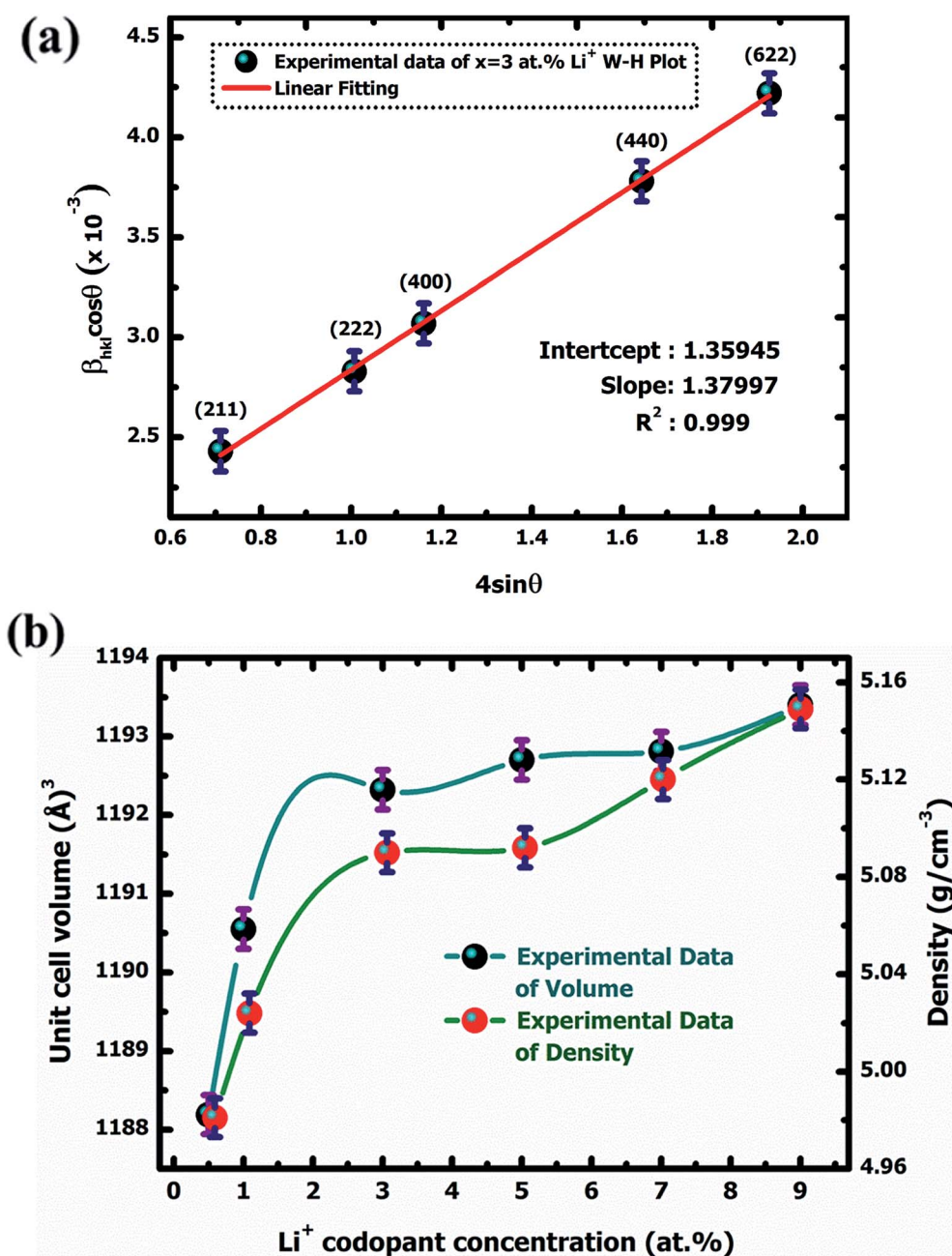$$D = \frac{k\lambda}{\beta \cos \theta} \tag{1}$$

Fig. 2 W–H plot of Y_2O_3:4 at% Eu^{3+}, xLi^+ (a) $x = 3$ at% nanophosphor (b) variation of unit cell volume and density with Li^+ codoping concentration.

where $k = 0.9$ is the dimensionless shape factor (Scherrer constant), $\lambda = 1.5405$ Å is the wavelength of X-ray radiation used, β is the Full width at half maximum (FWHM) in radians, θ is the Bragg angle in degrees of diffraction peaks. Based on this relation, the calculated average crystallite sizes of Y_2O_3:4 at% Eu^{3+}, xLi^+ ($x = 0.5, 1, 3, 5, 9$ at%) nanophosphors were obtained within nanoscale range from 50 to 55 nm. Further, the effective lattice strain (ε) associated with nanophosphors were calculated by Williamson–Hall (W–H) plots using the relation:[18]

$$\beta_{hkl} \cos \theta = \frac{k\lambda}{D} + 4\varepsilon \sin \theta \qquad (2)$$

where β_{hkl} represents full width at half maximum (FWHM) in radians and D represents the effective crystallite size present in the sample. The effective lattice strain values were obtained from the slope of the linear fit by plotting $4 \sin \theta$ along the x-axis versus $\beta_{hkl} \cos \theta$ along the y-axis. Fig. 2(a) the Williamson–Hall plots of Y_2O_3:4 at% Eu^{3+}, xLi^+ ($x = 3$ at%) nanophosphors, where five major peaks with miller indices (211), (222), (400), (440) and (622) were used. It is observed that the lattice strain increases with increasing Li^+ concentration. The lower value of lattice strain (ε) indicates a lower level of lattice imperfection present in the crystal.[19] The diffraction peaks were also observed slightly shifts towards the lower angle (2θ) side which indicates the variations in the lattice parameters can occur of the nanophosphors. This variation of lattice parameters (a) is calculated using the formula as follows:[20]

$$a = \frac{\lambda\sqrt{h^2 + k^2 + l^2}}{2 \sin \theta} \qquad (3)$$

The calculated lattice parameters were found to increase with increasing doping Eu^{3+} and codoping Li^+ concentration. This is understandable that the ionic radius of Eu^{3+} (1.06 Å) has larger than those of Y^{3+} (1.01 Å) and Li^+ (0.9 Å). The orderly increases lattice parameter indicates that the ions were occupied in the Y^{3+} site in the lattice. The unit cell volume also increased with increasing co-doping Li^+ concentration due to the lattice expansion in the crystal. All the qualitative structural parameters of the prepared samples are listed in Table 1.

3.1.2. Quantitative X-ray diffraction (XRD) analysis. Quantitative X-ray diffraction (XRD) analysis of Y_2O_3:4 at% Eu^{3+}, xLi^+ ($x = 0.5, 1, 3, 5, 7, 9$ at%) nanophosphors was performed by the Rietveld refinement method.[21] All the structural parameters were evaluated through the FullProf Suite crystallographic program using powder XRD data. The obtained structural refined parameters are summarized in Table 2. The Pseudo-Voigt function $i.e.$, the summation of a Gaussian and Lorentzian function was utilized to fit various parameters to the data point. The patterns were typically fitted with parameters such as backgrounds, cell parameters; scale factor, zero shiftings, shape and width of the peaks, atomic coordinates, isothermal temperature factors, and asymmetric factors. The refinement result exhibited that nanophosphors have a body-centered cubic (I) phase with point group symmetry $m\bar{3}$. The fitting parameters R_{wp}, R_{ex}, GoF, R_p, R_{Bragg}, R_F, and χ^2 were also shown a good agreement with the observed and calculated XRD

Table 1 Structural parameters of Y_2O_3:4 at% Eu^{3+}, xLi^+ ($x = 0.5, 1, 3, 5, 7, 9$ at%) nanophosphors

Nanophosphor	Li$^+$ concentration (at%)	2θ (°)	Miller indices hkl Calculated	Miller indices hkl Observed	Lattice constants a (Å) Calculated	Lattice constants a (Å) Observed	Crystallite size (nm) Debye–Scherrer	Lattice strain ε ($\times 10^{-3}$) (W–H)	Volume of unit cell a^3 (Å)
Y_2O_3:4 at% Eu^{3+}, x Li$^+$	$x = 0.5$	29.21	(2 2 2)	(2 2 2)	10.604	10.582	50.08	1.177	1184.95
	$x = 1$	29.18	(2 2 2)	(2 2 2)	10.604	10.593	51.02	1.214	1188.65
	$x = 3$	29.16	(2 2 2)	(2 2 2)	10.604	10.600	52.85	1.379	1191.01
	$x = 5$	29.15	(2 2 2)	(2 2 2)	10.604	10.603	53.95	1.442	1192.02
	$x = 7$	29.14	(2 2 2)	(2 2 2)	10.604	10.607	54.97	1.478	1193.37
	$x = 9$	29.13	(2 2 2)	(2 2 2)	10.604	10.610	55.26	1.495	1194.38

Table 2 Reitveld refinement parameters of Y_2O_3:4 at% Eu^{3+}, xLi^+ (x = 0.5, 1, 3, 5, 7, 9 at%) nanophosphors

Nanophosphor	Li$^+$-concentration (at%)	Rietveld refinement parameters								
		R_{wp}	R_{exp}	GoF	R_p	R_{Bragg}	R_F	χ^2	Cell volume a^3 (Å)	Density g cm^{-3}
Y_2O_3:4 at% Eu^{3+}, x Li$^+$	$x = 0.5$	23.8	19.64	1.21	36.8	6.45	6.07	1.47	1188.19	5.149
	$x = 1$	24.4	23.05	1.05	44.0	4.57	4.27	1.12	1190.55	5.120
	$x = 3$	22.3	22.26	1.00	41.5	2.84	3.29	1.00	1192.32	5.092
	$x = 5$	22.3	18.55	1.20	37.9	8.59	6.69	1.53	1192.70	5.090
	$x = 7$	23.0	21.43	1.07	41.0	4.46	4.26	1.15	1192.81	5.024
	$x = 9$	21.8	19.95	1.09	33.9	4.93	4.09	1.20	1193.04	4.978

patterns. The observed, calculated, and difference between observed and calculated XRD patterns for nanophosphors are shown in Fig. 3(a), (b), (c), (d), (e), and (f), respectively. The quality of refinement data was examined by the lower values of the goodness of fit (GoF) which is obtained by the ratio of expected and weighted profile of R factors i.e., GoF = R_{wp}/R_{exp}. For the best refinement, GoF must approach less than two. In this case, GoF values were found to be 1.21, 1.01, 1.00, 1.20, 1.07, and 1.09 respectively which confirmed our fitting is best. By observing unit cell volume and density it shows increases continuously with increasing co-dopant Li$^+$ concentration which is due to the substitution of Li$^+$ to the host Y_2O_3 in increasing order from (0.5–9 at%). Fig. 2(b) shows the variation of unit cell volume and density with increasing Li$^+$ codoping concentration.

All the crystal structures were modeled through a three-dimensional visualization program called Visualization for Electronic and Structural Analysis (VESTA) using Y_2O_3:4 at% Eu^{3+}, xLi^+ (x = 7 at%) nanophosphors refinement data.[22] The refined parameters such as occupancy, atomic coordinates, phase, space group, and lattice parameters were used to model these structures. Fig. 4(a) illustrates the crystal structure of cubic yttrium(III) oxide (Y_2O_3). It contains 32 cations which are the summation of two partially distributed cation Y^{3+}(1) located at 24d site (Wyckoff position) with C_2 (noncentrosymmetric) symmetry and Y^{3+}(2) located at 8b (Wyckoff position) site with $C_{3i}(S_6)$ (centrosymmetric) inversion symmetry of the crystallographic lattice. Oxygen ions were occupied at the 48e site (Wyckoff position) of the Y_2O_3 host lattice. In the Y_2O_3 crystal structure, both the cations $Y^{3+}(C_2)$ and $Y^{3+}(C_{3i})$ have made six-fold octahedral coordination with oxygen thus forming the [YO$_6$] octahedron structure having 8 faces, 12 edges and 6 vertices are shown in Fig. 4(b) and (c). The observed bond angles and bond length of this octahedron are shown in Fig. 4(d) and (e). The obtained Y–O average bond length and polyhedral volume were accordingly 2.264 Å, 14.17 Å^3 corresponds to $Y^{3+}(C_2)$ and 2.232 Å, 14.72 Å^3 corresponds to $Y^{3+}(C_{3i})$ symmetry site of the lattice.

3.1.3. Fourier transform infrared spectroscopy (FTIR). Fig. 5(a) depicts the FTIR spectra of Y_2O_3:4 at% Eu^{3+}, xLi^+ (x = 0.5, 1, 3, 5, 7, 9 at%) nanophosphors. The observed spectra were recorded in the middle infrared region ranges from 4000–400 cm^{-1} using potassium bromide (KBr) pellet techniques. Fig. 5(b) shows the magnified FTIR spectra of Y_2O_3:4 at% Eu^{3+}, 7

at% Li$^+$ nanophosphor. The weak absorption band at 3616 cm^{-1} was detected due to the symmetric O–H stretching vibration (ν) of the (OH) hydroxyl group.[23] This is attributed to the H_2O molecule, as KBr absorbed the moisture from the air during the pellet preparation or absorbed water by nanophosphors materials from the ambient atmosphere due to its high surface to volume ratio. The strong absorption bands at 1648, 1563, 1410, 1348, and 1262 cm^{-1} are attributed to C–O stretching vibration (ν) and the bands at 1050, 1018, and 925 cm^{-1} are attributed to C–O bending vibration (δ), respectively.[24] These bands were due to the absorption of CO_2 on the surface of the nanophosphors from the ambient atmosphere or residue of carbon in the prepared nanophosphor. It shows that nanomaterials were decomposed completely and no additional hydrogen is remaining there. The weaker metal–oxygen stretching bands observed at 511 and 501 cm^{-1} were assigned to the Y–O lattice vibration of cubic Y_2O_3.[25] This indicates no other phase or impurities were present in the prepared sample that is pure and crystalline. By the addition of Li$^+$ concentration in the Y_2O_3:4 at% Eu^{3+} as a codopant, it enhances the intensity and improves the crystallinity of the sample which was consistent with the XRD results.

3.1.4. Morphological studies. Fig. 6 shows the typical higher resolution Transmission Electron Micrograph (TEM) of Y_2O_3:4 at% Eu^{3+}, xLi^+ (a) x = 0.5, (b) x = 1 (c) x = 3 (d) x = 5 (e) x = 7 and (f) x = 9 nanophosphors, respectively. The calculated average nanoparticle size estimated from TEM images was around 80 to 90 nm, which is greater than the crystallite size obtained from qualitative XRD analysis and indicating the agglomeration of the sample. By observing the micrograph, it is found that the sizes of nanoparticles were varied with the codoping concentration of Li$^+$ ions and it shows good agreement with XRD analysis. The selected area electron diffraction (SAED) pattern shows multiple diffraction spots ordered in rings, which confirms good crystallization and polycrystalline in the nature of the nanophosphor as shown in Fig. 6(g). The diffraction rings corresponding to (211), (222), (400), (440), and (622) planes were indexed to cubic Y_2O_3, and is in accordance with the XRD results. The high-resolution TEM image shows clear lattice fringes of the prepared nanophosphor which indicating high crystallinity with polycrystalline in nature of the sample as shown in Fig. 6(h). The lattice fringes shows interplanar spacing of 4.32 Å, 3.74 Å, 2.65 Å, 1.87 Å, 1.89 Å and 1.21 Å consistent with the plane d_{211} = 4.32 Å, d_{222} = 3.74 Å, d_{400} =
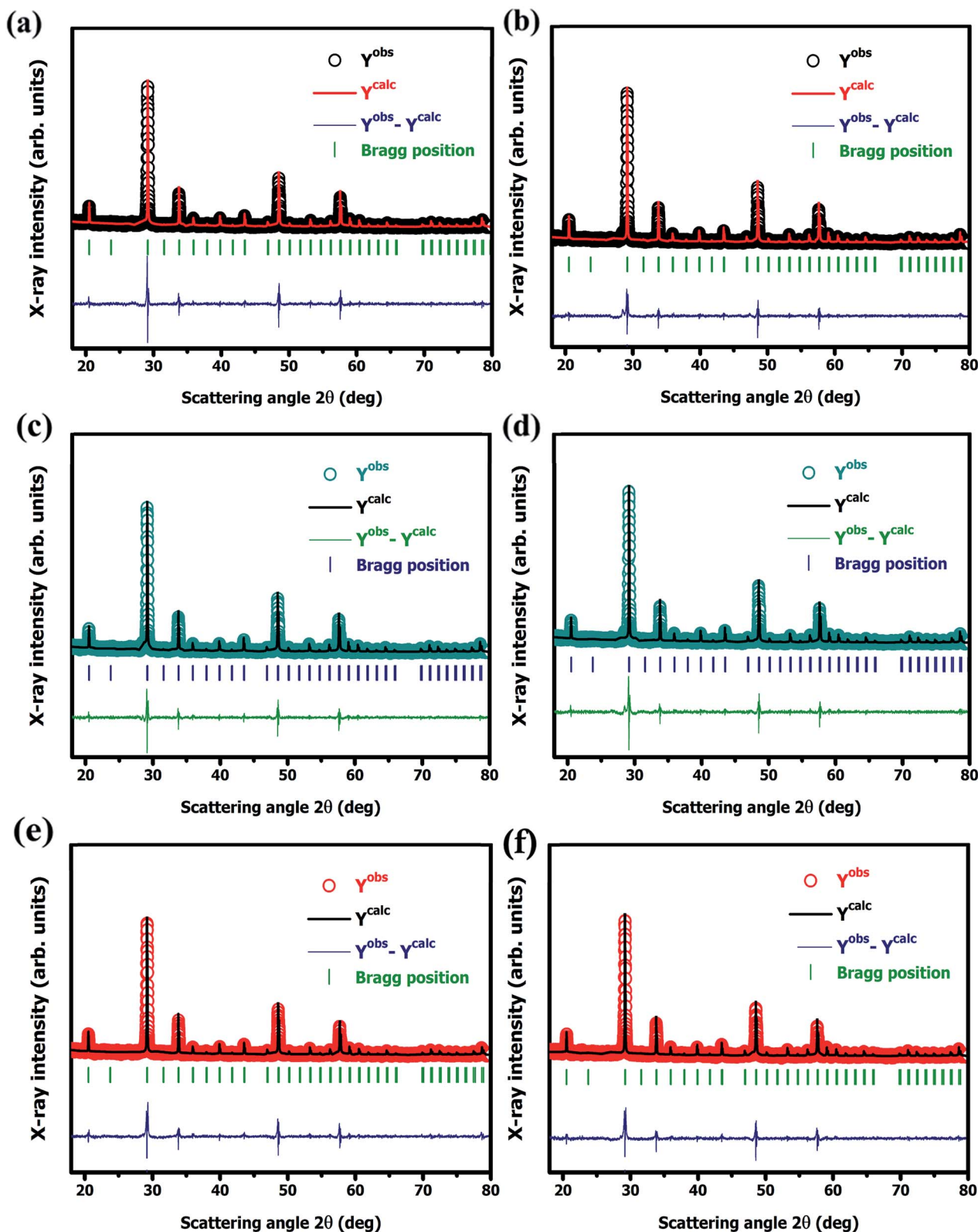
Fig. 3   Rietveld refined XRD pattern of Y_2O_3:4 at% Eu^{3+}, $x$$Li^+$ nanophosphors (a) $x = 0.5$ at%, (b) $x = 1$ at% (c) $x = 3$ at%, (d) $x = 5$ at%, (e) $x = 7$ at%, and (f) $x = 9$ at%, respectively.

2.65 Å, $d_{440} = 1.87$ Å, $d_{622} = 1.89$ Å and $d_{662} = 1.21$ Å values from the ICDD card no. 41-1105 respectively, of the cubic Y_2O_3 structure.

3.2.   Optical characterization

3.2.1.   Photoluminescence (PL) study. Fig. 7(a) represents the photoluminescence (PL) excitation spectra of Y_2O_3:4 at%
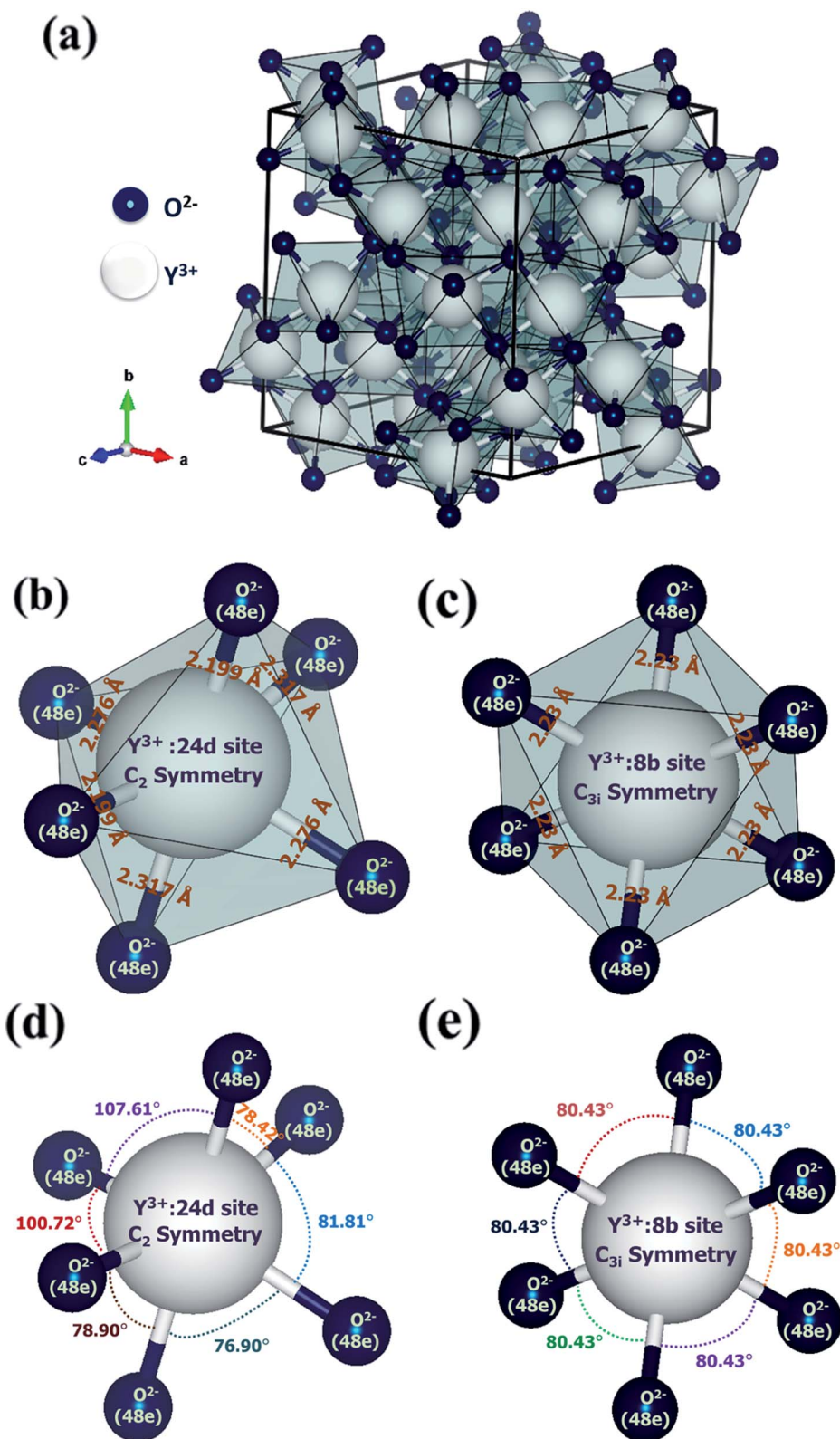
Fig. 4 Crystal structure of cubic yttrium(III) oxide (Y_2O_3): (a) unit cell with coordination polyhedra and octahedral coordination with oxygen of cation Y^{3+}. (b) Polyhedron of 24d site with C_2 symmetry and interatomic distances are presented in Å. (c) Polyhedron of 8b site with $C_{3i}(S_6)$ symmetry and interatomic distances are presented in Å. (d) A ball and stick model of 24d site with C_2 symmetry and bond angles are presented in deg. (e) A ball and stick model of 8b site with $C_{3i}(S_6)$ symmetry and bond angles are presented in deg.
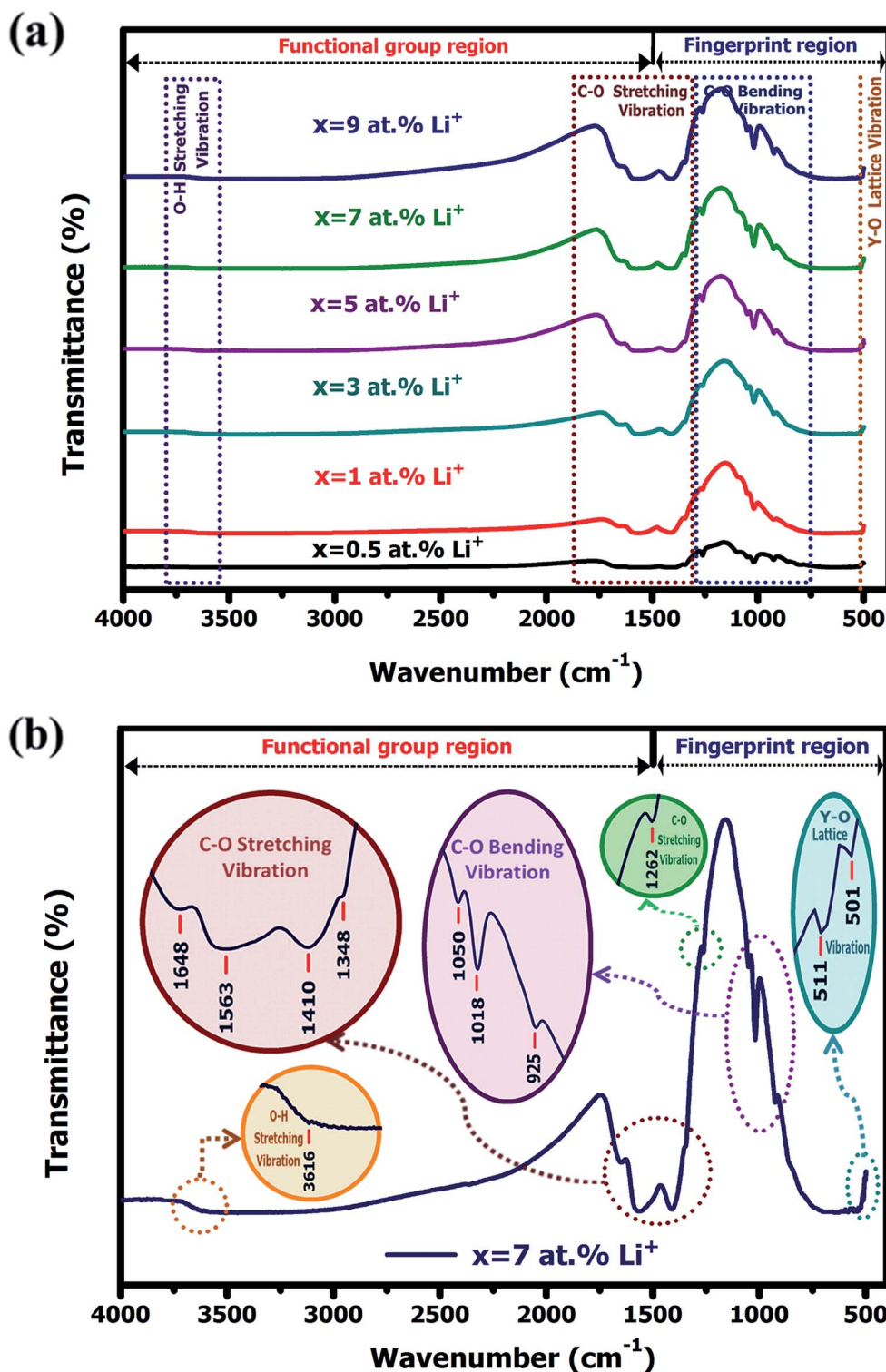
Fig. 5 (a) FTIR spectra of Y_2O_3:4 at% Eu^{3+}, xLi^+ ($x = 0.5$, 1, 3, 5, 7, 9 at%) nanophosphors. (b) The magnified FTIR spectra of Y_2O_3:4 at% Eu^{3+}, 7 at% Li^+ nanophosphor.

Eu^{3+}, xLi^+ ($x = 0.5$, 1, 3, 5, 7, 9 at%) nanophosphors. The excitation spectra were obtained by monitoring emission wavelength at 612 nm, corresponding to $^7F_0 \rightarrow {}^5D_2$ transition of Eu^{3+} which exhibits three broad absorption bands at 254, 393, and 466 nm respectively. The strong band exhibited at 254 nm was due to the charge transfer from 2p orbital of O^{2-} to the 4f orbital of Eu^{3+} ion in Y_2O_3:Eu^{3+}.[26] The charge transfer transition occurred because the $4f^6$ configuration of Eu^{3+} tends to gain an electron from 2p orbital O^{2-} for achieving stable $4f^7$ half-filled shell configuration.[27] The higher two absorption bands at 393,
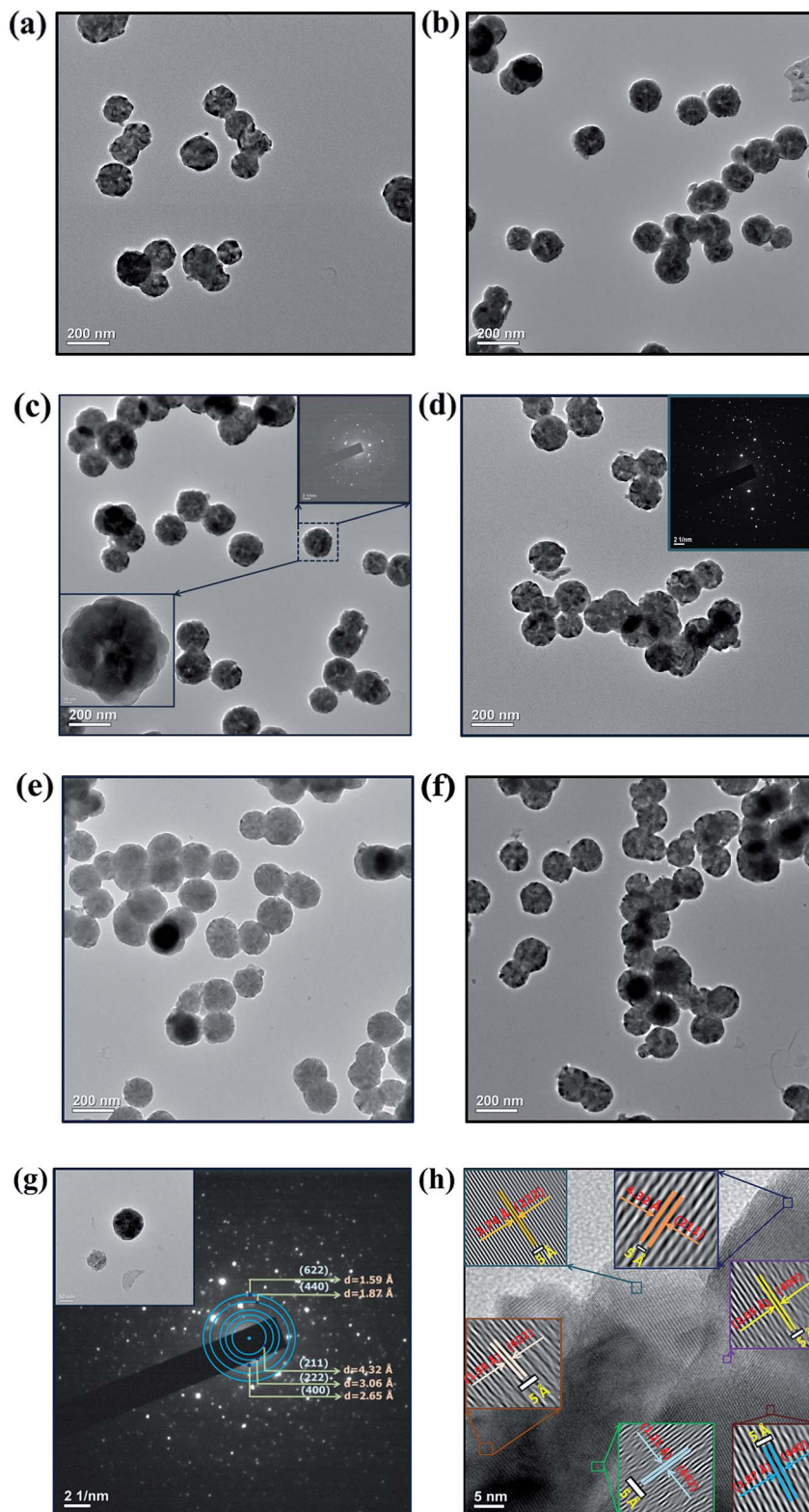
Fig. 6 HR-TEM Images of Y_2O_3:4 at% Eu^{3+}, xLi^+ (a) $x = 0.5$ at%, (b) $x = 1$ at%, (c) $x = 3$ at%, (d) $x = 5$ at%, (e) $x = 7$ at%, (f) $x = 9$ at% nanophosphors. (g) The magnified HR-TEM image and SAED pattern analysis of $x = 9$ at% prepared crystalline sample. (h) Lattice fringes of $x = 9$ at% samples corresponds to cubic yttrium(III) oxide (Y_2O_3).

466 nm were ascribed to the $^7F_0 \rightarrow {}^5L_6$ and $^7F_0 \rightarrow {}^5D_2$ transition of Eu^{3+} ion. On increasing the Li^+ co-doping concentration the absorption band intensity reveals increases up to 7 at% and then gradually decreases though further increase of Li^+ concentration. This shows that higher co-doping concentration can enhance the excited absorption intensity of the
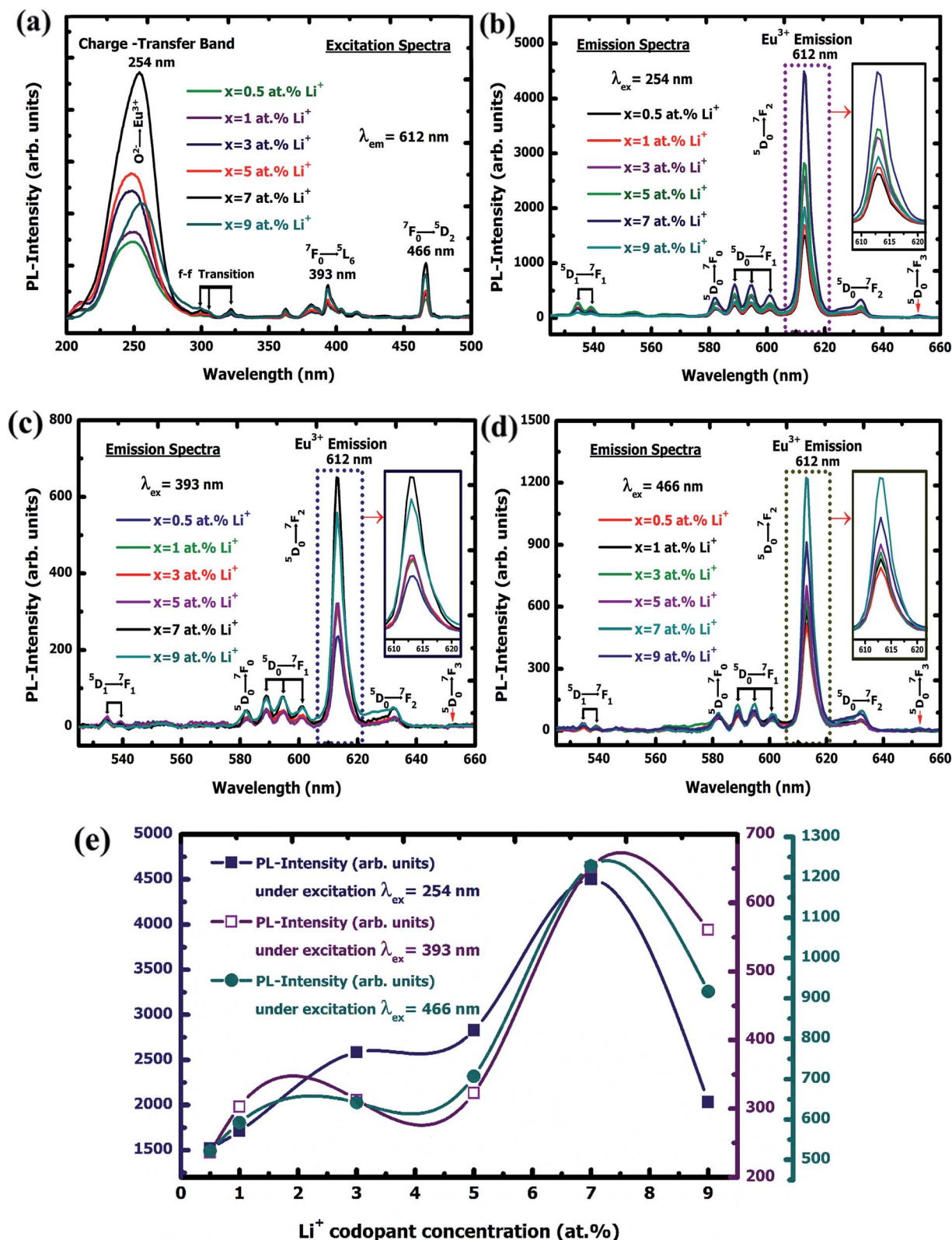
Fig. 7 (a) PL excitation spectra of Y_2O_3:4 at% Eu^{3+}, $x$$Li^+$ (x = 0.5, 1, 3, 5, 7, 9 at%) nanophosphors. PL emission spectra of Y_2O_3:4 at% Eu^{3+}, $x$$Li^+$ (x = 0.5, 1, 3, 5, 7, 9 at%) nanophosphors under excitation (b) λ_{exc} = 254 nm, (c) λ_{exc} = 393 nm and (d) λ_{exc} = 466 nm, respectively. (e) PL emission intensity variation of Y_2O_3:4 at% Eu^{3+}, $x$$Li^+$ (x = 0.5, 1, 3, 5, 7, 9 at%) nanophosphors under excitation λ_{exc} = 254, 393, and 466 nm, respectively.

**Table 3** Analysis of photoluminescence highest emission intensity variation of Y_2O_3:4 at% Eu^{3+}, xLi^+ (x = 0.5, 1, 3, 5, 7, 9 at%) nanophosphors with respect to various excitation

Nanophosphor	Excitation wavelength (nm)	Emission wavelength (nm)	Transition	Maximum intensity (arb. units)	Ratio (arb. units)
Y_2O_3:4 at% Eu^{3+}, x Li$^+$	λ_{ex} = 254	λ_{em} = 612 (red)	$^5D_0 \rightarrow {}^7F_2$	4490.00	254 : 393 = 6.90
	λ_{ex} = 393	λ_{em} = 612 (red)	$^5D_0 \rightarrow {}^7F_2$	650.21	254 : 466 = 3.67
	λ_{ex} = 466	λ_{em} = 612 (red)	$^5D_0 \rightarrow {}^7F_2$	1223.03	466 : 393 = 1.88

nanophosphor at a certain level. The less intense bands at 299, 305 and 321 nm were also detected in longer wavelength region attributed to $4f^6$–$4f^6$ transitions of Eu^{3+} ion.[28,29] The increased of absorption intensities probably due to the electron transition to CTB promotes under higher Li^+ concentration. When the Li^+ is added into the nanocrystals there will be the charge balance and this can be maintained by introducing of oxygen vacancies. By increasing codoping concentration Li^+ along with the amount of Li^+ ion presence at the substitutional and interstitial sites also increased. This results, increase of crystal defects around the activator lanthanide ions and create the lattice imperfection into the crystal. Thereby, the stark levels in the emission spectrum show the large splitting, which leads to enhance the emission intensity.[30] Thus, the absorption intensity of the nanophosphor is enhanced with codoping concentration. Fig. 7(b)–(d) shows photoluminescence emission spectra of Y_2O_3:4 at% Eu^{3+}, xLi^+ (x = 0.5, 1, 3, 5, 7, 9 at%) nanophosphors excited by λ_{ex} = 254, 393 and 466 nm respectively. Where the impact of Li^+ ion on the photoluminescence emission band

intensity of prepared nanophosphors are studied in detail. The emission spectra exhibit peaks at ∼534 and 538 nm were attributed to the hypersensitive electric dipole $^5D_1 \rightarrow {}^7F_1$ transition of Eu^{3+} ion. This indicates the thermalisation takes place within $^5D_1$ multiplet due to the stark splitting.[31,32] The emission band observed at 582 nm was attributed to a $^5D_0 \rightarrow {}^7F_0$ electric dipole transition,[33] which specifies that Eu^{3+} ion does not occupy in a centrosymmetric site of the host lattice.[34] It occupies only C_3 and C_s noncentrosymmetric sites of the following symmetries: C_s, C_1, C_2, C_3, C_4, C_6, C_{2v}, C_{3v}, C_{4v}, and C_{6v} according to electric dipole selection rule.[35] The emission band intensity at ∼588, 594, and 600 nm is ascribed to the magnetic dipole transition of $^5D_0 \rightarrow {}^7F_1$ at 8b crystallographic cation site and $S_6(C_{3i})$ (centrosymmetric) symmetry of Y_2O_3 (25%) host lattice.[36] The most prominent red emission band at 612 nm and a small band at 632 nm were attributed to the $^5D_0 \rightarrow {}^7F_2$ hypersensitive forced electric dipole transition of Eu^{3+} ion at 24d crystallographic cation site and C_2 (noncentrosymmetric) symmetry of Y_2O_3 (75%) host lattice.[37] This indicates that Eu^{3+}
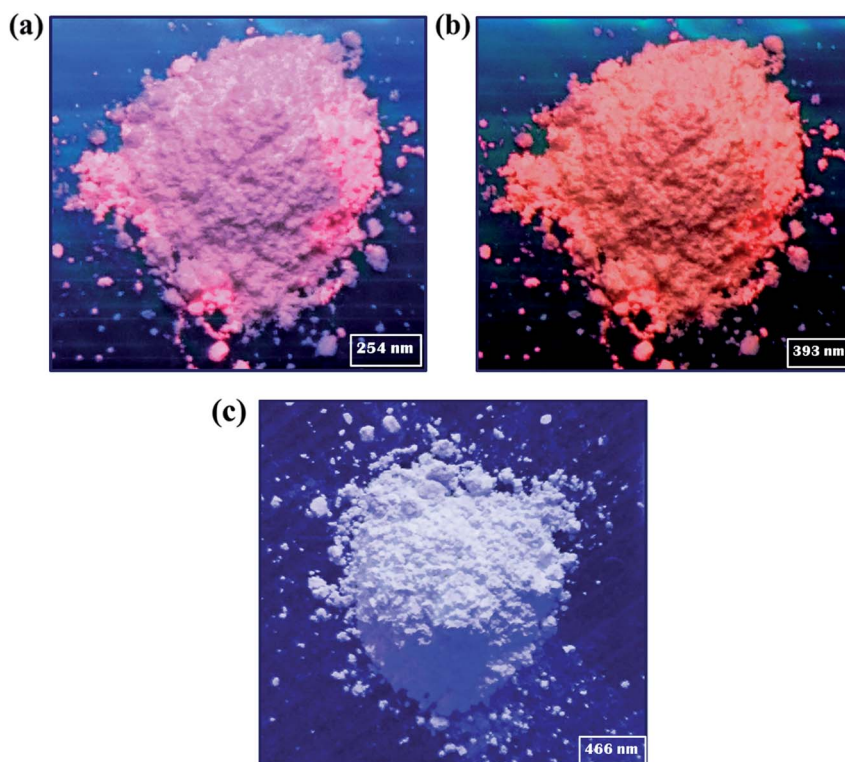
Fig. 8 Digital photographs of nanophosphor under different excitation wavelength, such as (a) 254 nm (b) 393 nm and (c) 466 nm, respectively.
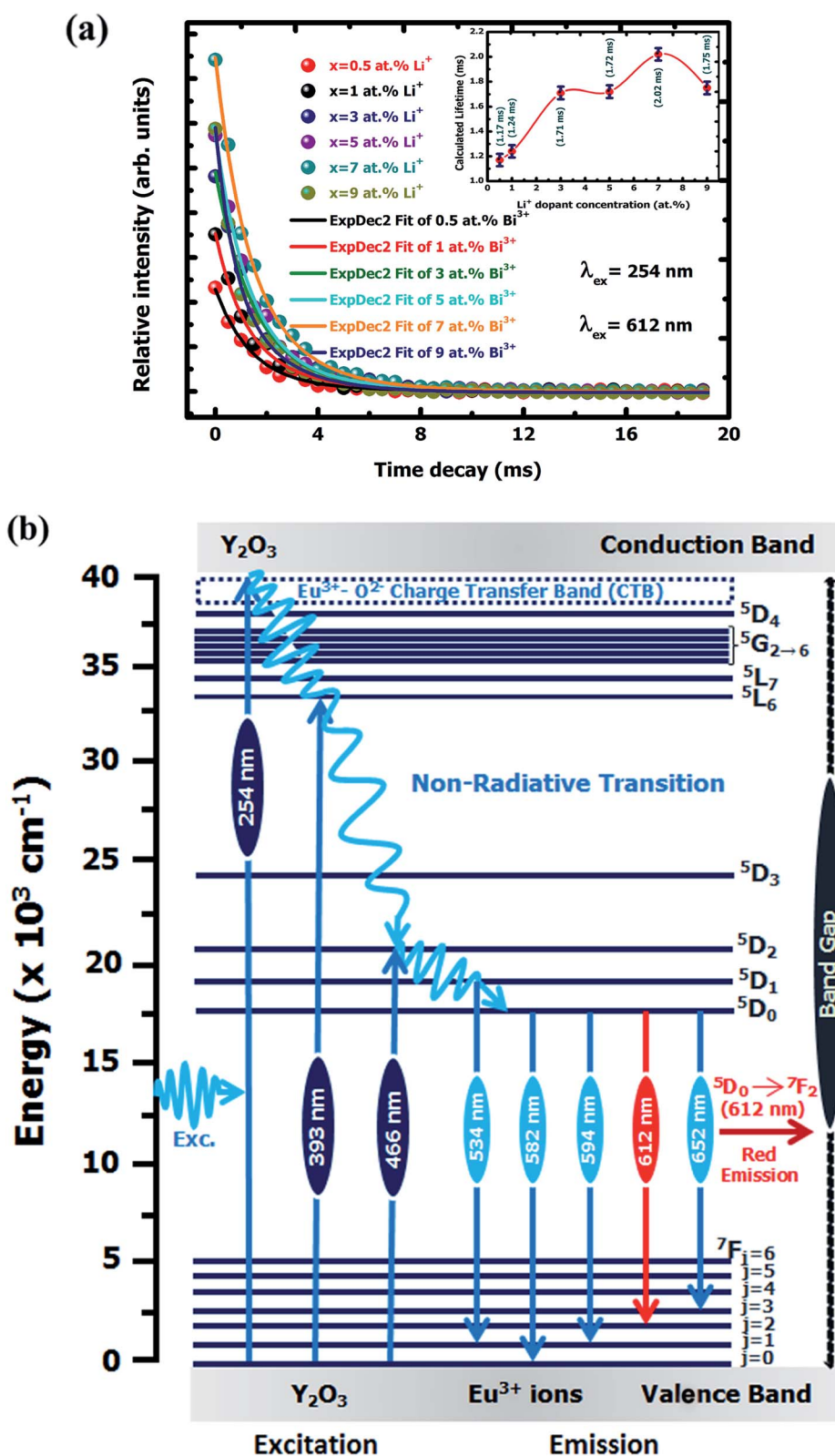
Fig. 9 (a) PL lifetime decay curves of Y_2O_3:4 at% Eu^{3+}, $x$$Li^+$ (x = 0.5, 1, 3, 5, 7, 9 at%) nanophosphors. (b) Schematic energy level diagram for Y_2O_3:4 at% Eu^{3+}, $x$$Li^+$ (x = 0.5, 1, 3, 5, 7, 9 at%) nanophosphors.

ions were occupying in two separate positions in the crystallographic lattice. The other weak emission band exhibit at 652 nm corresponding to the electric dipole or quadrupole and the

magnetic dipole is a forbidden transition of $^5D_0 \rightarrow {}^7F_3$, according to Judd–Ofelt theory.[38] This is because of J-mixing, where the wave function of $^7F_3$ state mixes with another

$^7F_{j=2,4,6}$ state.[39] These narrow emission bands were revealed due to the shielding effect of 4f electrons by 5s and 5p in the outer shell in the Eu^{3+} ion.[40] By observing all the red emission bands under various excitations were varies with different Li^+ co-doping concentration. The emission intensities were enhanced with the increased Li^+ concentration up to 7 at% and then gradually decreases though a further increase of Li^+ concentration. This is ascribed to the flux effect, improved the crystallinity and growth of the crystallite size caused by the Li^+ ion.[41] The obtained maximum enhanced intensity of prepared nanophosphor is 4490, 1223.03, 650 (a.u.) concerning excitation wavelengths λ_{ex} = 254, 393, 466 nm respectively. Where the highest emission intensity band was observed under 254 nm excitation as compare to others. This is due to the charge transfer between O^{2-}–Eu^{3+} ion. The ionic radius of Li^+ is smaller compare to the Eu^{3+} and Y^{3+} ion. Thereby it can easily enter the host lattice and can occupy both the substitutional and interstitial sites. When the codoping of Li^+ is occupied in lattice sites substitutionally it shows the decrease of emission intensity of Y_2O_3:Eu^{3+}, Li^+ nanophosphor, whereas if Li^+ ion occupies in the lattice sites interstitially it shows the enhancement of the emission intensity.[42] After entering the interstitial site, Li^+ ion can bring the host lattice expansion, thus the variation of lattice constant is occurs. In the case of 0.5, 1, 3, 5, and 9 at% co-doping concentration, Li^+ ions dominant substitutional occupation leads to low luminescent intensity. But, in 7 at% codoping concentration, the interstitial occupation of Li^+ appears. This causes to enhance the higher luminescence emission intensity at 7 at% than the other concentrations. The enhancement of emission intensity is also indicated the presence of lattice imperfection in the crystal system. An increment of lattice imperfection indicates the increase of oxygen vacancies created by co-dopant Li^+ ion. The strong mixing of Li^+ ion act as a sensitizer which leads to effective energy transfer in a charge-transfer state by recombining of deeply trapped charges and photogenerated electrons from the conduction band.[43] It will decrease luminescence quenching centers at the surface of nanophosphors and increases crystallinity, thereby enhancing the emission band intensity.[44,45] With increasing of Li^+ concentration the oxygen vacancy also substantially increases, which will demolish the emission intensity. Thereby the increase of emission intensity holds up to 7 at% above this it declines even though Li^+ concentration increases further. By comparing all the highest emission band intensity it is found that the most intense emission band excited by 254 nm shows a 6.9 times enhancement than the emission band intensity excited by 393 nm and 3.67 times enhancement than the emission band intensity excited 466 nm. Therefore, the highest intense band may be applicable as a prominent red light emission band for WLEDs fabrication. The second highest emission band intensity under excitation 466 nm shows 1.88 times enhancement than the emission band intensity excited by 393 nm. Thus, it shows that the enhancement of emission band intensity also depends on the variations of excitation wavelength. All these variations of the highest emission intensity plot under various excitation wavelengths are shown in Fig. 7(e) and the calculated ratios are shown in Table 3. The reason for choosing 4 at% Eu^{3+} doped in Y_2O_3 nanoparticles is that it shows optimal emission band intensity as compared to other concentration such as 2, 4, 5, 6, 7, 8, 10, 15 and 20 at%, respectively. It exhibited the prominent red emission band at 610 nm due to the $^5D_0 \rightarrow {}^7F_2$ transition of Eu^{3+} ion under 250 nm excitation annealed at 500 °C.[14] This indicates the particular concentration based nanophosphor could be a potential candidate to generate the red color for further use as a red component to construct white light color in WLEDs fabrication. Fig. 8(a)–(c) shows the digital photograph of nanophosphor under different excitation wavelength, such as 254, 393 and 466 nm, respectively. Fig. 9(b) represents the energy level diagram for Y_2O_3:4 at% Eu^{3+}, xLi^+ (x = 0.5, 1, 3, 5, 7, 9 at%) nanophosphors. The nanophosphors were excited under three different wavelengths such as 254, 393, and 466 nm respectively. Where the electrons located at ground state ($^7F_{j=0}$) of Eu^{3+} ion are promoted to an excited state by absorbing corresponds excitation energy. The excited electrons transfer their location to the $^5D_1$ and $^5D_0$ energy levels by releasing the energy non-radiatively. Finally, the excited electron moves to the ground state by emitting red light under $^5D_1 \rightarrow {}^7F_1$ and $^5D_0 \rightarrow {}^7F_{j=0,1,2,3}$ transitions of Eu^{3+} ion. Therefore, it is confirmed that this red-emitting nanophosphor could be a potential candidate for WLEDs fabrication.

3.2.2 Lifetime study. Fig. 9(a) shows the photoluminescence decay behaviour of $^5D_0 \rightarrow {}^7F_2$ (λ_{em} = 612 nm) transition of Eu^{3+} for Y_2O_3:4 at% Eu^{3+}, xLi^+ (x = 0.5, 1, 3, 5, 7, 9 at%) nanophosphors excited at 254 nm. All these monitored curves were excellently fitted by a second-order exponential function as follows:[46]

$$I(t) = I_0 + A_1 \exp(-t/\tau_1) + A_2 \exp(-t/\tau_2) \tag{4}$$

Table 4 Photoluminescence decay lifetime of Y_2O_3:4 at% Eu^{3+}, xLi^+ (x = 0.5, 1, 3, 5, 7, 9 at%) nanophosphors

Nanophosphor	Li^+-concentration (at%)	Excitation wavelength (nm)	Emission wavelength (nm)	Transition	τ_1 (ms)	τ_2 (ms)	Lifetime τ_{avg} [ms]
Y_2O_3:4 at% Eu^{3+}, x Li^+	x = 0.5	λ_{ex} = 254	λ_{em} = 612 (red)	$^5D_0 \rightarrow {}^7F_2$	2.86	0.88	1.17
	x = 1	λ_{ex} = 254	λ_{em} = 612 (red)	$^5D_0 \rightarrow {}^7F_2$	1.30	0.43	1.24
	x = 3	λ_{ex} = 254	λ_{em} = 612 (red)	$^5D_0 \rightarrow {}^7F_2$	1.12	2.34	1.71
	x = 5	λ_{ex} = 254	λ_{em} = 612 (red)	$^5D_0 \rightarrow {}^7F_2$	2.18	0.92	1.72
	x = 7	λ_{ex} = 254	λ_{em} = 612 (red)	$^5D_0 \rightarrow {}^7F_2$	3.31	1.34	2.02
	x = 9	λ_{ex} = 254	λ_{em} = 612 (red)	$^5D_0 \rightarrow {}^7F_2$	2.39	1.14	1.75

where I_0 and $I(t)$ denoted the luminescence emission intensity at time 0(s), and t(s), respectively, t is time constant, τ_1 and τ_1 represents the fast and slow decay times for exponential components, A_1 and A_2 are assigned fitting parameters constants. The fast and slow decay is assigned non-radiative and radiative transition of Eu^{3+} ion of the nanophosphor. The average lifetimes for the studied nanophosphors were evaluated by using the relation:[47]

$$\tau_{avg} = (A_1\tau_1^2 + A_2\tau_2^2)/(A_1\tau_1 + A_2\tau_2) \tag{5}$$

Thus, the τ_1, τ_2 and average decay times τ_{avg} values of Y_2O_3:4 at% Eu^{3+}, $x$$Li^+$ (x = 0.5, 1, 3, 5, 7, 9 at%) nanophosphors are listed in Table 4. It is observed that the average lifetimes of the nanophosphors are varying with the co-doping concentration of Li^+ ions. The average lifetimes increase with an increase of Li^+ concentration up to x = 7 at% and gained a maximum value of 2.02 ms then slightly decreased though further increase the Li^+ concentration. This is because of the flux effect caused by Li^+ ion, which improved the high crystallinity of the sample. The Li^+ concentration also reduced luminescence-quenching centers at the surface of nanophosphors with improved crystallinity, thereby increases the average lifetime. The addition of different Li^+ concentrations also affected the surroundings of Eu^{3+} ion under $^5D_0 \rightarrow {}^7F_2$ transition that causes the variation of an average lifetime.

3.2.3. Photometric characterization. The Commission Internationale de l'Eclairage (CIE) 1931 chromaticity diagram has been used to specify the luminescence color of any nanophosphor. The colors are represented as a chromaticity color coordinates (x, y) and correlated color temperature (CCT) in the color space calculated from PL emission spectra through color calculator software. These chromaticity coordinates are calculated by using the three dimensionless color matching functions $\bar{x}(\lambda)$, $\bar{y}(\lambda)$ and $\bar{z}(\lambda)$, respectively.[48] The degree of stimulation is used to specified power-spectral density $P(\lambda)$ and can be obtained by using the three equations:[49]

$$X = \int_\lambda \bar{x}(\lambda)P(\lambda)d\lambda \tag{6}$$

$$Y = \int_\lambda \bar{y}(\lambda)P(\lambda)d\lambda \tag{7}$$

$$Z = \int_\lambda \bar{z}(\lambda)P(\lambda)d\lambda \tag{8}$$

where X, Y, and Z are three tristimulus values that provide the stimulation values for standard RGB colors to match the color $P(\lambda)$. The chromaticity coordinates x, y, and z are calculated from the ratio of the tristimulus values (XYZ) by using the following relations:

$$x = \frac{X}{X + Y + Z} \tag{9}$$

$$y = \frac{Y}{X + Y + Z} \tag{10}$$

$$z = \frac{Z}{X + Y + Z} \tag{11}$$

Generally, only two coordinates values of these are independent because $x + y + z = 1$ regardless of the assigned value of X, Y and Z. Hence CIE 1931 chromaticity diagram selected x and y coordinates to represent the color. Fig. 10 shows the chromaticity diagram for the Y_2O_3:4 at% Eu^{3+}, $x$$Li^+$ (x = 0.5, 1, 2, 3, 5,

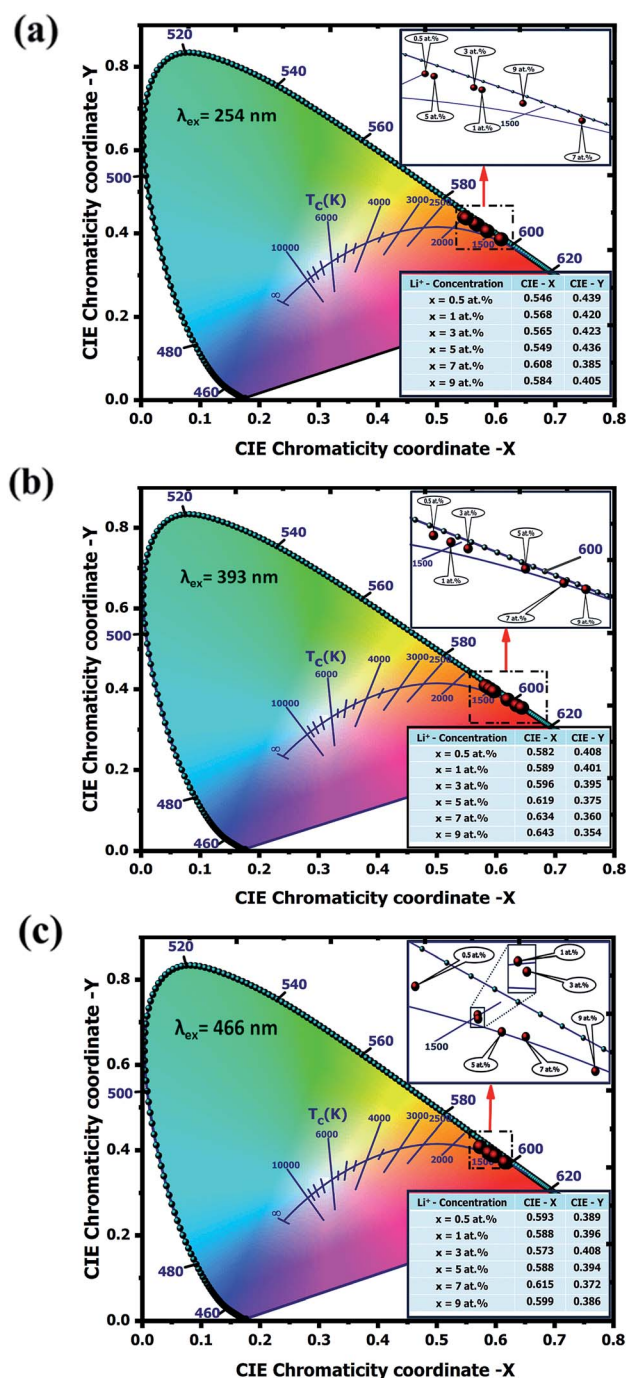Fig. 10 The CIE 1931 chromaticity diagram of Y_2O_3:4 at% Eu^{3+}, $x$$Li^+$ (x = 0.5, 1, 3, 5, 7, 9 at%) nanophosphors excited by (a) 254 nm (b) 393 nm and (c) 466 nm, respectively.

Table 5 The CIE parameters of Y_2O_3:4 at% Eu^{3+}, $x$$Li^+$ (x = 0.5, 1, 3, 5, 7, 9 at%) nanophosphors excited by 254, 393 and 466 nm, respectively

Nanophosphor	Excitation wavelength (nm)	Li^+-concentration (at%)	CIE-chromaticity coordinates		CCT (K)	Color purity (%)	CIE color
			X	Y			
Y_2O_3:4 at% Eu^{3+}, x Li^+	λ_{ex} = 254	x = 0.5	0.546	0.439	2000.36	95.58	Red
		x = 1	0.568	0.420	1765.30	96.96	Red
		x = 3	0.565	0.423	1793.56	98.18	Red
		x = 5	0.549	0.436	1961.10	96.11	Red
		x = 7	0.608	0.385	1639.12	98.56	Red
		x = 9	0.584	0.405	1652.62	96.98	Red
Y_2O_3:4 at% Eu^{3+}, x Li^+	λ_{ex} = 393	x = 0.5	0.582	0.408	1666.08	96.59	Red
		x = 1	0.589	0.401	1634.31	97.20	Red
		x = 3	0.596	0.395	1620.95	97.83	Red
		x = 5	0.619	0.375	1713.88	98.89	Red
		x = 7	0.634	0.360	1946.06	98.11	Red
		x = 9	0.643	0.354	2117.04	99.65	Red
Y_2O_3:4 at% Eu^{3+}, x Li^+	λ_{ex} = 466	x = 0.5	0.593	0.389	1620.24	100	Red
		x = 1	0.588	0.396	1627.74	96.39	Red
		x = 3	0.573	0.408	1693.05	92.37	Red
		x = 5	0.588	0.394	1625.19	93.39	Red
		x = 7	0.615	0.372	1716.13	100	Red
		x = 9	0.599	0.386	1625.01	91.60	Red

7 at%) nanophosphors under excitation wavelength (a) 254 nm, (b) 393 nm and (c) 466 nm respectively. The CIE color coordinates (x, y) values of this nanophosphor with various Li^+ concentrations have been calculated by using the PL emission spectra data. It is observed from the figure, all the positions of color coordinates under different excitation wavelengths were located in the red region of the color space.

The quality of the light source has been examined in terms of kelvin (K) based correlated color temperature (CCT) evaluated from chromaticity coordinates. The CCT represents the temperature of a closest Planckian blackbody radiator, whose operating point is closest to the chromaticity point on the CIE chromaticity diagram. The CCT values were calculated using McCamy's empirical formula:[50]

$$CCT = 449n^3 + 3525n^2 + 6823.3n + 5520.33 \quad (12)$$

where $n = (x - x_e)/(y_e - y)$ is an inverse slope line, (x, y) represents the color coordinates and the $x_e = 0.332$ and $y_e = 0.185$ are chromaticity epicentre. The calculated CCT values under different excitation wavelengths were found to vary within the range of 1620.24 K to 2117.04 K which belongs in the red region. The variation of CCTs is observed due to the different Li^+ codoping concentrations. Apart from color coordinates, color purity also expressed the colorific behavior of emitted light and can be estimated using the following relation:[51]

$$\text{Color purity} = \frac{\sqrt{(x_s - x_i)^2 + (y_s - y_i)^2}}{\sqrt{(x_d - x_i)^2 + (y_d - y_i)^2}} \times 100\% \quad (13)$$

where (x_s, y_s) are the color coordinates of a studied sample, (x_d, y_d) are the color coordinates of the dominant wavelength calculated from the intersection point of the connecting line

with spectrum locus which is drawn from the white point through a color representing coordinates point of the chromaticity diagram and $(x_i = 0.333, y_i = 0.333)$ are the color coordinates of the CIE white illuminant point. Based on the eqn (13) the color purity of synthesized phosphors were found to be more than 91% which indicates Li^+ codoped Y_2O_3:4 at% Eu^{3+} nanophosphor is one of the important candidates to produced red emission. The calculated chromaticity color coordinates, CCT, and color purity values of prepared nanophosphors are listed in Table 5. Hence, the detailed analysis of the nanophosphor affirms that the prepared materials are more suitable for the fabrications of the white light-emitting diode as the red-emitting nanophosphor.

4. Conclusions

In summary, we have presented the effect of Li^+ on tunable Y_2O_3:4 at% Eu^{3+} red-emitting nanophosphors by structural and luminescence study. The X-ray diffraction pattern shows the formation of pure body-centered cubic phase of Y_2O_3 with $Ia\bar{3}$ (Number 206, Z = 16) space group without impurity peaks and which confirms there is no effect of Li^+ ion on it. The crystallite size was found to be in the range of 50–55 nm calculated by the Debye–Scherrer formula. The quantitative Rietveld refinement exhibited the nanophosphor has a body-centered cubic (I) phase with point group symmetry $m\bar{3}$. Higher resolution TEM and FTIR study confirm the nanophosphors are good crystallinity with polycrystalline in nature. The PL emission intensity is found greatly depends on the concentration of Li^+ ion. With increasing the Li^+ concentration the emission intensities are enhanced up to 7 at% and then declines with the further increase of Li^+ concentration is due to the flux effect. The most intense emission band was observed at 612 nm ascribed to the

$^5D_0 \rightarrow {}^7F_2$ transition of Eu^{3+} ion upon 254, 393, and 465 nm excitations. The emission band excited at 254 nm shows the highest enhancement than the other that is 6.9 times higher enhances than the emission intensity excited by 393 nm and 3.67 times enhances than the emission intensity excited by excited 466 nm respectively. The highly enhanced luminescence intensity is due to the flux effect of improved crystallinity, variations in the concentration of oxygen vacancy, and increases in optical volume caused by Li^+ ion. Besides, Li^+ ion can improve the average lifetime of $^5D_0 \rightarrow {}^7F_2$ transition, which may be the cause of variation of sensitizer concentration and the radiative transition rate. The CIE chromaticity diagram shows the position of calculated color coordinates; CCTs under different excitation wavelengths were located in the red region. Hence, all the results indicate that Y_2O_3:4 at% Eu^{3+}, xLi$^+$ (x = 0.5, 1, 2, 3, 5, 7 at%) nanophosphors can be used as a red-emitting nanophosphor for WLEDs applications.

Conflicts of interest

The author declares there is no conflicts of interest in the current research.

Acknowledgements

References

1 M. I. Martinez-Rubio, T. G. Ireland, G. R. Fern, J. Silver and M. J. Snowden, *Langmuir*, 2001, **17**, 7145–7149.

2 W.-C. Chien, Y.-Y. Yu and C.-C. Yang, *Mater. Des.*, 2010, **31**, 1737–1741.

3 J. H. Zhang, Z. D. Hao, J. Li, X. Zhang, Y. Luo and G. Pan, *Light: Sci. Appl.*, 2015, **4**, 239–244.

4 A. M. Khachatourian, F. Golestani-Fard, H. Sarpoolaky, C. Vogt, E. Vasileva, M. Mensi, S. Popov and M. S. Toprak, *J. Lumin.*, 2016, **169**, 1–8.

5 C. Liang, X. Huang and W. Huang, *J. Mater. Sci.: Mater. Electron.*, 2018, **29**, 11271–11279.

6 Q. Zhang, X. Wang, X. Ding and Y. Wang, *Inorg. Chem.*, 2017, **56**, 6990–6998.

7 Z. Sun, Y. Zhou and M. Li, *J. Mater. Res.*, 2008, **23**, 732–736.

8 M. Peng, X. Yin, P. A. Tanner, C. Liang, P. Li, Q. Zhang and J. Qui, *J. Am. Ceram. Soc.*, 2013, **96**, 2870–2876.

9 L. Wang, N. Liao, L. Shi, H. Jia, P. Du, N. Wang, Z. Xi and D. Jin, *Electrochem. Solid-State Lett.*, 2010, **13**, E19–E21.

10 L. Yongqing, Z. Lingyun, D. Zhenxiang, Z. Ganhong, Z. Yanan and M. Yongqing, *Rare Met. Mater. Eng.*, 2017, **46**, 1524–1529.

11 A. Pramanik, S. Biswas, C. S. Tiwary, P. Kumbhakar, R. Sarkar and P. Kumbhakar, *J. Colloid Interface Sci.*, 2020, **565**, 326–336.

12 Q. Wang, Y. Gao, B. Wang, Y. Guo, U. Ahmad, Y. Wang, Y. Wang, S. Lu, H. Li and G. Zhou, *J. Mater. Chem. C*, 2020, **8**, 4343–4349.

13 S. Sadeghi, S. K. Abkenar, C. W. Ow-Yang and S. Nizamoglu, *Sci. Rep.*, 2019, **9**, 10061.

14 L. R. Singh, R. S. Ningthoujam, V. Sudarsan, I. Srivastava, S. D. Singh, G. K. Dey and S. K. Kulshrestha, *Nanotechnology*, 2008, **19**, 055201.

15 H. M. Rietveld, *J. Appl. Crystallogr.*, 1969, **2**, 65–75.

16 J. Rodríguez-Carvajal, *FULLPROF: A Rietveld refinement pattern matching analysis program*, Laboratory Léon Brillouin (CEA-CNRS): Gif-sur-Yvette Cedex, France, 2011, https://www.ill.eu/sites/fullprof/.

17 S. T. Tan, B. J. Chen, X. W. Sun, W. J. Fan, H. S. Kwok, X. H. Zhang and S. J. Chua, *J. Appl. Phys.*, 2005, **98**, 013505.

18 G. K. Williamson and W. H. Hall, *Acta Metall.*, 1953, **1**, 22–31.

19 U. Pal, D. Samantha, S. Ghorai and A. K. Chaudhuri, *J. Appl. Phys.*, 1993, **74**, 6368–6374.

20 B. D. Cullity, *Elements of X-ray Diffraction*, Addison-Wesley Publishing Company, Inc., Reading, MA, 1978, 2nd edn.

21 M. Ferrari and L. Lutterotti, *J. Appl. Phys.*, 1994, **76**, 7246–7255.

22 K. Momma and F. Izumi, VESTA: a three-dimensional visualization system for electronic and structural Analysis, *J. Appl. Crystallogr.*, 2008, **41**, 653–658.

23 R. S. Ukare, G. D. Zade, B. Deva Prasad Raju and S. J. Dhoble, *Optik*, 2016, **127**, 1871–1878.

24 D. Kumar, M. Sharma and O. P. Pandey, *Opt. Mater.*, 2014, **36**, 1131–1138.

25 R. Hari Krishna, B. M. Nagabhushana, H. Nagabhusana, N. Suriya Murthy, S. C. Sharma, C. Shivakumara and R. P. S. Chakradhar, *J. Phys. Chem. C*, 2013, **117**, 1915–1924.

26 X. Bai, H. Song, L. Yu, L. Yang, Z. Liu, G. Pan, S. Lu, X. Ren, Y. Lei and L. Fan, *J. Phys. Chem. B*, 2005, **109**, 15236–15242.

27 Z. G. Wei, L. D. Sun, C. S. Liao, X. C. Jiang, C. H. Yan, Y. Tao, X. Y. Hou and X. Ju, *J. Appl. Phys.*, 2003, **93**, 9783–9788.

28 G. Jia, H. You, Y. Song, Y. Huang, M. Yang and H. Zhang, *Inorg. Chem.*, 2010, **49**, 7721–7725.

29 J. Yang, Z. Quan, D. Kong, X. Liu and J. Lin, *Cryst. Growth Des.*, 2007, **7**, 730–735.

30 N. Dhananjaya, H. Nagabhushana, B. M. Nagabuushana, B. Rudraswamy, C. Shivakumara and R. P. S. Chakradhar, *J. Alloys Compd.*, 2011, **509**, 2368–2374.

31 A. Ćirić, S. Stojadinović, M. G. Brik and M. D. Dramićanin, *Chem. Phys.*, 2020, **528**, 110513.

32 A. K. Singh, K. P. O'Donnell, P. R. Edwards, D. Cameron, K. Lorenz, M. J. Kappers, M. Boćkowski, M. Yamaga and R. Prakash, *Appl. Phys. Lett.*, 2017, **111**, 241105.

33 J. S. Bae, B. K. Moon, J. H. Jeong, S. S. Yi and J. H. Kim, *J. Appl. Phys.*, 2005, **98**, 043513.

34 F. P. Du, Y. Nakai, T. Tsuboi, Y. L. Huang and H. J. Seo, *J. Mater. Chem.*, 2011, **21**, 4669–4678.

35 X. Y. Chen and G. K. Liu, *Solid State Chem.*, 2005, **178**, 419–428.

36 M. Maitric, B. Antic, M. Balanda, D. Rodic and M. L. Napijalo, *J. Phys.: Condens. Matter*, 1997, **9**, 4103–4111.

37 J. Silver, M. I. Martinez-Rubio, T. G. Ireland and R. Withnall, *J. Phys. Chem. B*, 2001, **105**, 7200–7204.

38 K. A. Gschneidner and L. R. Eyring, *Handbook on the Physics and Chemistry on Rare-Earths*; North-Holland Amsterdam, 1997.

39 C. Cascales, J. Fernández and R. Balda, *Opt. Express*, 2005, **13**, 2141–2152.

40 X. Li, Q. Li, Z. Xia, L. Wang, W. Yan, J. Wang and R. I. Boughton, *Cryst. Growth Des.*, 2006, **6**, 2193–2196.

41 N. Liao, L. Shi, H. Jia, X. Yu, D. Jin and L. Wang, *Inorg. Mater.*, 2010, **46**, 1325–1329.

42 Y. Yan, W. Zhang, B. Ren, L. Zhong and Y. Xu, *Ionics*, 2016, **23**, 869–875.

43 S. Yi, J. S. Bae, B. K. Moon and J. H. Jeong, *Appl. Phys. Lett.*, 2002, **81**, 3344–3346.

44 J. Y. Cho, Y. R. Do and Y. Huh, *Appl. Phys. Lett.*, 2006, **89**, 131915.

45 J. S. Bae, J. H. Jeong, K. S. Shim, B. K. Moon, S. Yi, J. H. Kim, Y. S. Kim and J. S. Lee, *Appl. Surf. Sci.*, 2006, **252**, 4564–4568.

46 C. Liang, X. Huang and W. Huang, *J. Mater. Sci.: Mater. Electron.*, 2018, **29**, 11271–11279.

47 C. K. Lin, M. L. Pang, M. Yu and J. Lin, *J. Lumin.*, 2005, **114**, 299–306.

48 Q. Y. Zhang, K. Pita, W. Ye and W. X. Que, *Chem. Phys. Lett.*, 2002, **351**, 163–170.

49 K. V. Krishnaiah, K. P. Kumar and C. K. Jayasankar, *Mater. Express*, 2013, **3**, 61–70.

50 C. S. McCamy, *Color Res. Appl.*, 1992, **17**, 142–144.

51 Y. C. Fang, S. Y. Chu, P. C. Kao, Y. M. Chuang and Z. L. Zeng, *J. Electrochem. Soc.*, 2011, **158**, J1–J5.